Title

Defect-Driven Redox Interplay on Anatase TiO2: Surface-Structure Dependent Activation for CO2 Hydrogenation Catalysis

Journal

Journal of the American Chemical Society, 147(47)

ISSN

0002-7863

Authors

Chen, Xiaobo
Lee, Yonghyuk
Hong, Seunghwa
et al.

Publication Date

2025-11-26

DOI

10.1021/jacs.5c06076

Defect-driven redox interplay on anatase TiO_2: surface-structure dependent activation for CO_2 hydrogenation catalysis

Xiaobo Chen[1,8], Yonghyuk Lee[2], Seunghwa Hong[3], Emily K. Schroeder[3], Sabrina M. Gericke[4], Greg D. Barber[5], Zhihengyu Chen[6], Sarah A. Hesse[6], Christopher J. Tassone[6], Robert M. Rioux[5,7], Phillip Christopher[3], Simon R. Bare[6], Meng Li[4], Dmitri N. Zakharov[4], Anastassia N. Alexandrova[2], Ashley R. Head[4], Guangwen Zhou[8], Judith C. Yang[1,4*]

[1] Department of Chemical and Petroleum Engineering, University of Pittsburgh, Pittsburgh, Pennsylvania 15261, United States

[2] Department of Chemistry and Biochemistry, University of California, Los Angeles, Los Angeles, California 90095, United States

[3] Department of Chemical Engineering, University of California, Santa Barbara, California 93106, United States

[4] Center for Functional Nanomaterials, Brookhaven National Laboratory, Upton, New York 11973, United States

[5] Department of Chemical Engineering, Pennsylvania State University, University Park, Pennsylvania, 16802, United States

[6] SSRL, SLAC National Accelerator Laboratory, Menlo Park, California, 94025, United States

[7] Department of Chemistry, Pennsylvania State University, University Park, Pennsylvania, 16802, United States

[8] Department of Mechanical Engineering & Materials Science and Engineering Program, State University of New York at Binghamton, Binghamton, New York 13902, United States

Abstract

Titanium dioxide (TiO_2) is one of the most extensively studied oxides as an active catalyst or catalyst support, particularly in energy and environmental applications, but the atomistic mechanisms governing its dynamic response to reactive environments and their correlation to reactivity remain largely elusive. Using in-situ environmental transmission electron microscopy (ETEM), synchrotron X-ray diffraction (XRD), ambient-pressure X-ray photoelectron spectroscopy (AP-XPS), reactivity measurements, and theoretical modeling, we reveal the dynamic interplay between oxygen loss and replenishment of anatase TiO_2 under varying reactive conditions. Under

H_2 exposure, anatase TiO_2 undergoes surface reduction via lattice oxygen loss, forming Ti_3O_5. In contrast, CO_2 exposure induces oxygen replenishment, reversing stoichiometry. In mixed H_2/CO_2 environments, the reverse water-gas shift (RWGS) reaction proceeds selectively on stepped and high-indexed TiO_2 surfaces, whereas the thermodynamically stable TiO_2(101) surface remains inactive and intact. Critically, H_2 pre-treatment generates oxygen vacancies on TiO_2(101), transforming it into an active Ti_3O_5 or defect-rich surface that catalyzes RWGS. By corelating surface structure, defect dynamics, and gas-phase interactions, this work deciphers the competition between H_2-driven reduction and CO_2-driven oxidation pathways at the atomic scale. These insights establish defect engineering as a strategic lever to activate inert TiO_2 facets, advancing the design of adaptive catalysts for sustainable fuel synthesis technologies.

Keywords: Anatase TiO_2, O vacancy, Oxygen loss and replenishment, Reverse water-gas shift reaction, Surface reduction, In-situ TEM

* To who correspondence should be addressed: jyang1@bnl.gov

Introduction

Heterogeneous catalysts, particularly those consisting of oxide-supported metals or metal oxides, are essential for producing commodity chemicals and fuels. Key reactions such as CO_2 hydrogenation, the reverse water-gas shift (RWGS) reaction to methanol, and CO oxidation have been extensively investigated using catalytic systems like $Cu/ZnO/Al_2O_3$,[1] Ni/CeO_2,[2,3], Pt/CeO_2[4,5] Ni/TiO_2,[6–8] Rh/TiO_2,[9,10] Pt/TiO_2,[11] and Au/TiO_2[12,13]. While significant advancements have been made in identifying active sites and unraveling structure-reactivity relationships,[14,15] a fundamental atomic-scale understanding of dynamic surface and interfacial processes under reactive conditions, such as interfacial chemical reactions and metal-support interactions, remains elusive. A critical gap persists in the oversimplified view of oxide supports, which are often regarded merely as inert structural stabilizers or oxygen reservoirs, overlooking their intrinsic physicochemical properties and active participation in catalytic cycles.[16,17] This work focuses on elucidating the dynamic behavior of oxide supports themselves, aiming to uncover the atomic-scale mechanisms by which their surfaces and interfaces govern catalytic reactivity.

Anatase TiO_2 is widely utilized as an oxide support in heterogeneous catalysis, owing to its inherent reducibility and sub-stoichiometric composition under reducing conditions. Previous ETEM studies have revealed complex surface reconstructions and chemical dynamics on TiO_2 and other oxides under reactive environments,[18–20] highlighting the highly dynamic nature of metal oxides. These properties critically govern its physicochemical behavior and catalytic performance. Notable examples are metal atoms or nanoparticles loaded onto different anatase TiO_2 facets, which yield site-specific reactivity and stability due to their unique coordination environments.[21,22] Using anatase TiO_2 as a prototypical system, this study employs in-situ ETEM to capture real-time atomic-scale dynamics of the RWGS reaction on TiO_2 surfaces. By controlling CO_2/H_2 gas mixtures at operationally relevant temperatures and pressures, we track spatiotemporal evolution of atomic configurations, from surface restructuring to bulk transformations, under reactive conditions. Along with complementary synchrotron XRD, AP-XPS and reactivity measurements, we reveal the dynamic interplay of lattice oxygen loss and replenishment, as well as facet-dependent redox competition during catalysis.

Density Functional Theory (DFT) and machine-learning interatomic potentials (MLIPs) further map structural phase evolution across anatase surfaces under varying oxygen chemical potentials. These calculations

reveal that the (112) facet undergoes reduction more readily than the (101) facet. Electronic structure analysis demonstrates how surface reduction alters H and CO_2 adsorption/dissociation energetics, governing reactivity and driving oscillatory transitions between oxidized and reduced states during catalysis. Our findings highlight the crucial role of oxygen vacancies in modulating the catalytic reactivity of anatase TiO_2—a behavior further governed by surface orientations and defect structure. By bridging atomic-scale dynamics to macroscopic reactivity, this work establishes a framework for engineering oxide and oxide-supported catalysts with adaptive surfaces for chemical synthesis and energy conversion.

Results and Discussion

2.1 Structural and Chemical Evolutions of Anatase TiO_2 under Reactive Conditions

Anatase TiO_2 nanoparticles (NPs) (99.9% purity, ~ 30 nm average diameter) were purchased from Research Nanomaterials Inc. Brunauer-Emmett-Teller (BET) analysis yielded a surface area of 49.4 m^2/g using physical adsorption of N_2 at 77 K, corresponding to an estimated particle diameter of 28.8 nm (assuming anatase density: 4.23 g/cm^3). This aligns with TEM observations, which show an average particle diameter of ~ 31.5±2 nm (Supplementary Fig. S1). Prior to in-situ TEM experiments, NPs were pretreated in an O_2 environment ($pO_2 = 5\times10^{-3}$ Torr, 400 °C, 30 min)) to combust surface carbon contamination.

Figs. 1(a-f) depict a time-sequenced series of high-resolution TEM (HRTEM) images capturing the dynamic surface evolution of TiO_2 under alternating H_2 or CO_2 environments, prior to combining them for RWGS conditions. Initial O_2 pretreatment at 400 ºC produces a stoichiometric TiO_2 surface with ordered atomic columns, confirmed by the fast Fourier transform (FFT) in Fig. 1a. Subsequent exposure to 3×10^{-3} Torr H_2 at 500 °C induces progressive O loss, initiating at the surface and propagating inward (Fig. 1b, c). The advancing reduction front (marked by cyan dashed lines in Fig. 1) correlates with the formation of Ti_3O_5(312) lattice fringes (more examples in Supplementary Fig. S2, S3), consistent with lattice O removal under reducing conditions. The transition from TiO_2 to Ti_3O_5 is accompanied by a theoretical volume shrinkage ~ 10.2% (see calculation details in Supplementary information Section 2), reflecting the structural compaction associated with oxygen vacancy formation and lattice

reconfiguration. With the formation of Ti_3O_5 layer, the further reduction becomes increasingly limited and eventually halts at a critical thickness, because the following oxygen removal may become diffusion-limited, governed by the transport of oxygen vacancies through the existing Ti_3O_5 layer (see more examples and discussion in Supplementary information Fig. S2). This self-limiting behavior is further supported by temperature-programmed reduction (TPR) measurements (Fig. S4), which reveal two distinct H_2 consumption peaks at 410 °C and 590 °C. These peaks are attributed to surface and subsequent bulk reduction processes, respectively, underscoring the kinetically hindered, depth-dependent reduction of anatase TiO_2 under the H_2 reduction process at 500 °C.

Upon switching to 3×10^{-3} Torr CO_2, dissociative adsorption of CO_2 occurs on the reduced Ti_3O_5 surface, regenerating lattice O and releasing CO gas.[23] This O replenishment is evidenced by the resulting transformation of the Ti_3O_5 lattice into the TiO_2 structure, as seen in the recovery of well-defined atomic columns and relatively uniform image contrast in Figures 1(d–f). The interface between Ti_3O_5 and bulk TiO_2 (marked by cyan dashed lines) shifts from the bulk toward the surface (red arrows, Figs. 1(d-f)), driven by O reintegration. The corresponding FFTs confirm this structural healing, as reflections corresponding to Ti_3O_5(312) vanish (Fig. 1h). However, the reoxidation ($Ti_3O_5 \rightarrow TiO_2$) often remains incomplete, particularly in larger particles (see more examples in Fig. S6), due to kinetic limitations in oxygen transport. The smeared contrast at the center shown in Fig. 1(f) is consistent with residual reduced domains or defect-rich regions, indicating non-uniform reoxidation and potential trapping of vacancy clusters or defects within the particle core. Notably, the CO_2-driven healing process completes in ~ 60 s—three times faster than the time period (~200 s) of the Ti_3O_5 formation from H_2-induced reduction—underscoring the enhanced reactivity of the reduced Ti_3O_5 surface toward CO_2 dissociation. More experiments at 400 ºC corroborate this trend, demonstrating consistent CO_2 adsorption and dissociation on Ti_3O_5 (Supplementary Fig. S5). Figure 1(g) presents a representative HRTEM image (from in situ TEM observation in Supplementary Fig. S3) of the reduced anatase TiO_2 surface, revealing Ti_3O_5 formation viewed along the [352] zone axis. The corresponding FFT (Fig. 1h) aligns with Ti_3O_5 formation observed during H_2 exposure (Figs, 1a-c). Fig. 1i shows the atomic configurations of the parent TiO_2 and reduced Ti_3O_5, matching the crystallographic orientations in the HRTEM images in Fig. 1(g).

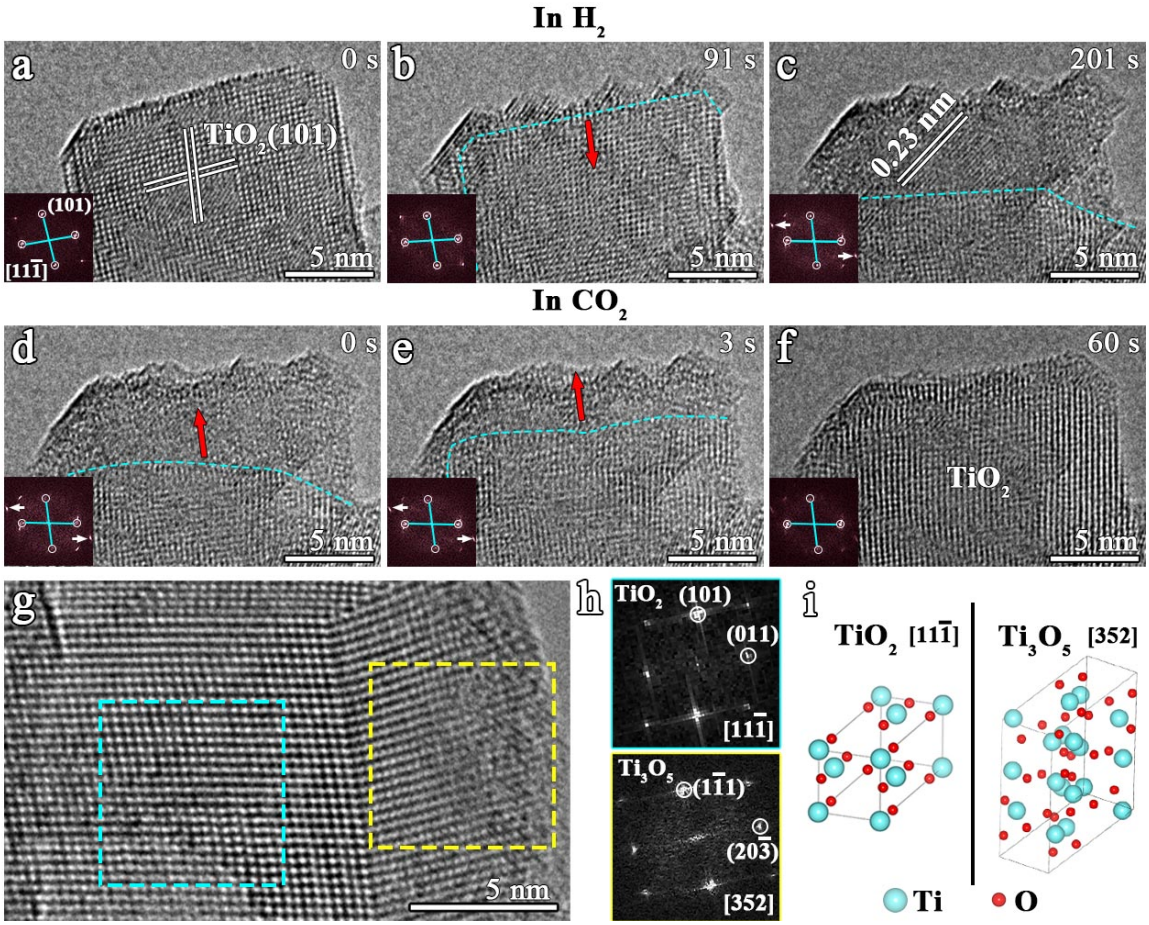

Figure 1. In-situ HRTEM imaging of TiO_2 reduction under H_2 and dynamic recovery under CO_2. **a-c**, Time-sequence HRTEM images capturing the progressive reduction of anatase TiO_2 to Ti_3O_5 (500 °C, ≈ 3×10^{-3} Torr H_2). The reduction front propagates from the surface into the bulk. **d-f**, Structural recovery of reduced TiO_2 under CO_2 (500 °C, ≈ 3×10^{-3} Torr CO_2). O replenishment drives the Ti_3O_5/TiO_2 interface (cyan dashed lines) from bulk to surface (red arrows), restoring stoichiometry and eliminating Ti_3O_5 diffraction features in FFTs. **g**, **h**, Representative HRTEM image and the corresponding FFT of reduced TiO_2 (500 °C, ≈ 2×10^{-4} Torr H_2), showing the TiO_2 bulk along the [11$\bar{1}$] zone axis and the Ti_3O_5 surface layer along the [352] zone axis. **i**, Schematic of the TiO_2 and Ti_3O_5 structures mirroring the lattice matching in (h).

To further investigate surface structural evolutions under varying reactive gas environments, in-situ high-angle annular dark-field scanning transmission electron microscopy (HAADF-STEM) and electron energy loss spectroscopy (EELS) were performed on anatase TiO_2 NPs exposed to O_2, H_2, and CO_2, respectively. Figures 2(a–c) present HAADF-STEM images under these conditions. O_2-treated TiO_2 exhibits uniform contrast (Fig. 2(a)),

while H_2 exposure induces localized contrast variations (bright/dark regions, white arrow in Fig. 2(b)), signaling O loss and structural evolution during reduction. Subsequent CO_2 exposure partially restores uniformity (Fig. 2(c)), reflecting O replenishment and structural reconstruction with kinetic limitations (see examples in Supplementary Fig. S6). EELS spectra from regions marked the dashed red boxes in Figs. 2(a-c) reveal chemical-state dynamics. Under H_2, Ti-$L_{2,3}$ and O K edges (Figs. 2d, e) show spectra shape changes (gray shaded regions), consistent with Ti^{4+} to Ti^{3+} reduction and O depletion.[24] Notably, a more reduced Ti oxidation state is observed at the outermost surface compared to the particle interior (see Supplementary Fig. S7). This is also supported by in-situ HRTEM observations in Figs. 1(a-c) and Fig. S8, with pronounced disordering on the outermost surface representing more heavily reduced, oxygen-deficient TiO_x regions. CO_2 exposure reverses these trends, restoring Ti^{4+} and O signatures (Figs. 2d, e), aligning with structural recovery shown in Figs. 1(a-f). Surface-sensitive AP-XPS measurements (Fig. 2(f)) corroborate these findings: reduction in H_2 introduces electronic states within the band gap (<3.2 eV), attributed to oxygen vacancy defect states,[25] consistent with the formation of Ti_3O_5 on the surface, while O_2 re-oxidation eliminates these features. Together, these results resolve the dynamic interplay of O loss and replenishment on TiO_2 surfaces, linking atomic-scale structural changes observed from in-situ TEM imaging to redox-driven chemistry.

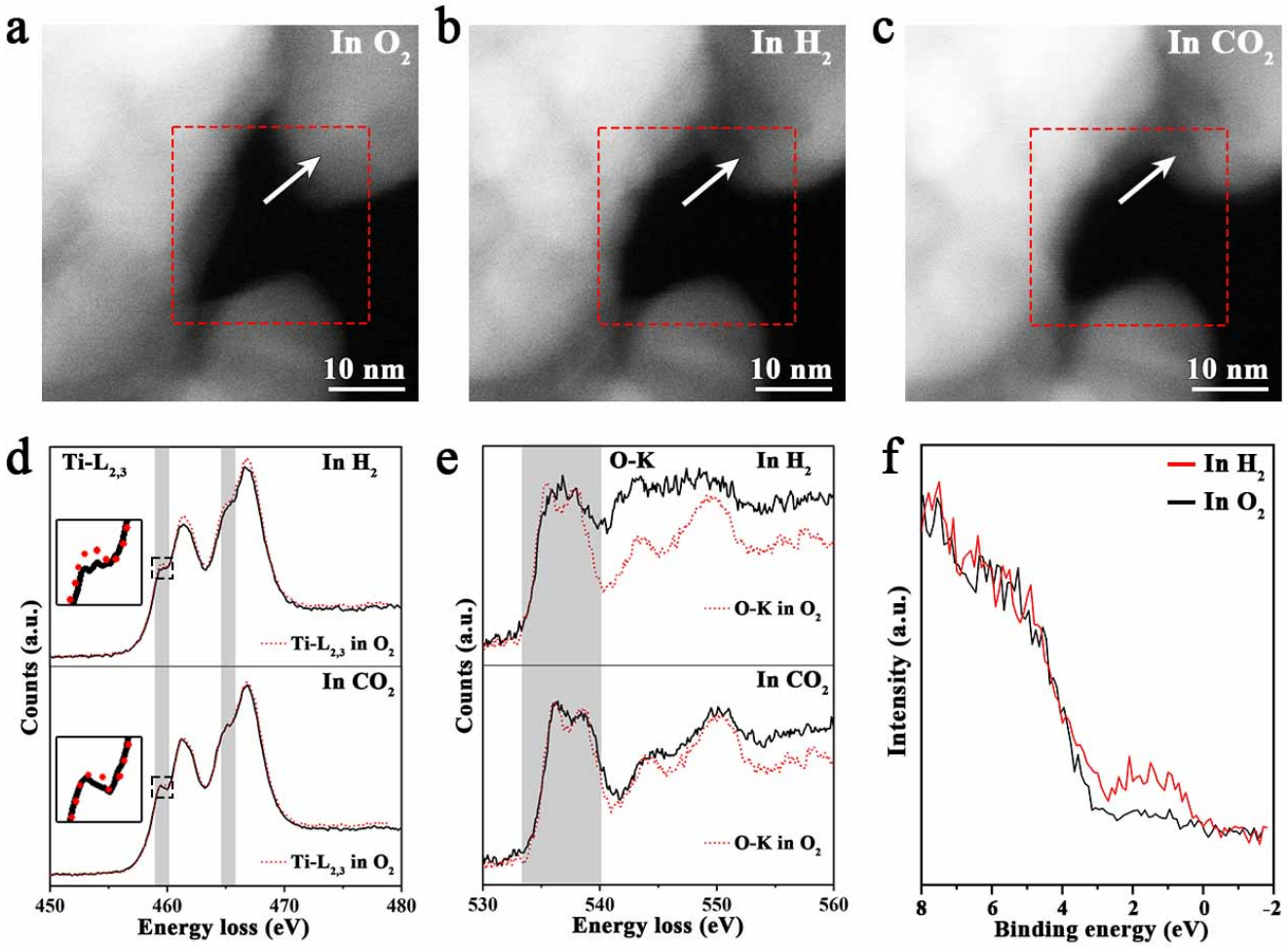

Figure 2. Redox-driven structural and chemical evolution of anatase TiO_2 surfaces under varying gas environments. **a**–**c**, In-situ HAADF-STEM images of TiO_2 NPs at 500 °C exposed to 5×10^{-3} Torr O_2, H_2, and CO_2, respectively. White arrows highlight localized contrast variations indicative of O loss during H_2 exposure and O replenishment under CO_2. **d**, **e**, EELS spectra of Ti $L_{2,3}$ and O K edges under alternating H_2 and CO_2 exposure. Under H_2, the Ti L_3 shoulder peak attenuation and O-K edge integrating signal indicate $Ti^{4+} \rightarrow Ti^{3+}$ reduction and O loss. CO_2 reverses these trends, restoring Ti^{4+} and O-K edge splitting. **f**, AP-XPS valence band spectra of TiO_2 under O_2 (400 °C, 2×10^{-3} Torr O_2, black) and H_2 (500 °C, 5×10^{-3} Torr H_2, red).

2.2 In-situ Environmental TEM Observations of RWGS Reaction Dynamics on Anatase TiO_2 Surface

To investigate the dynamic structure behaviors, we performed in-situ TEM experiments on O_2-pretreated TiO_2 NPs (500 °C for 30 min), following a CO_2/H_2 gas mixture (2×10^{-3} Torr CO_2, 6×10^{-3} Torr H_2). Fig. 3(a)

corresponds to the initial state, revealing well-defined (101), (112), and stepped (110) facets. Notably, slight atomic column displacements observed under O_2 (2×10^{-3} Torr, 400 °C) align with prior studies,[18–20,26–28] confirming O-adsorption-induced surface reconstruction. Time-resolved HRTEM images (Figs. 3(b-e)) capture dynamic surface evolution: (i) O loss and facet-specific activity: initial H_2/CO_2 exposure triggers O loss, inducing atomic displacements on the (110) facet and atom column merging on (112), while the (101) remains relatively stable (Fig. 3b). These changes are pronounced at undercoordinated (110) and (112) sites, prevalent at NP edges and corners. (ii) Oscillatory dynamics: progressive O exchange drives cyclic merging and splitting of atomic columns on the (112) facet (Fig. 3c), reflecting redox-driven lattice restructuring. Fig. 3d illustrates the intensity profiles of marked regions in Figs. 3c reveal atom column merging (uniform contrast) and splitting (peaks/valleys, red arrows), directly correlating with dynamic surface rearrangements.

Figure 3(e) highlights the dynamic evolution of the stepped TiO_2(110) facet marked by the dashed blue box in Fig. 3b. Cyan dots track morphological changes, revealing catalytic mass transport: new TiO_2 layers form on the left (indicative of surface growth), while the right exhibits semi-crystalline regions with disordered atomic columns display pronounced atom displacements. The appearance, disappearance, and movement of these atomic columns and pronounced displacements. These transient features arise from oscillatory O loss/gain dynamics at the gas-solid interface during CO_2 hydrogenation. Fig. 3(f) contrasts this activity with the stability of the TiO_2(101) facet. Real-time HRTEM imaging shows no structural reorganization on the (101) (more examples in Supplementary Fig. S9), indicating its limited catalytic role. Atomic step retraction initiates at the step edge (0 s image) on the TiO_2(101), followed by progressive receding (240 s image), evidenced by dismissing column contrast.

It is crucial to evaluate potential electron beam effects on in-situ TEM observations through control experiments, including "blank-beam" (Supplementary Fig. S10) and “vacuum annealing” (Supplementary Fig. S11) tests. These confirm that the electron beam dose rates used here do not measurably influence TiO_2 surface reaction dynamics (see Experimental methods for details). To complement the localized structural changes observed by in-situ TEM, synchrotron X-ray diffraction (XRD) is utilized to monitor bulk structural evolution during the RWGS reaction (Supplementary Fig. S12). XRD patterns of TiO_2—as-synthesized, O_2-pretreated, and post-reaction—confirm the stability of the anatase TiO_2. While in-situ HRTEM observations reveal dynamic surface restructuring,

XRD detects no bulk structural changes, underscoring that redox activity is confined to the surface. This surface-limited behavior aligns with reactivity measurements of pure anatase TiO_2 in the RWGS reaction, discussed below.

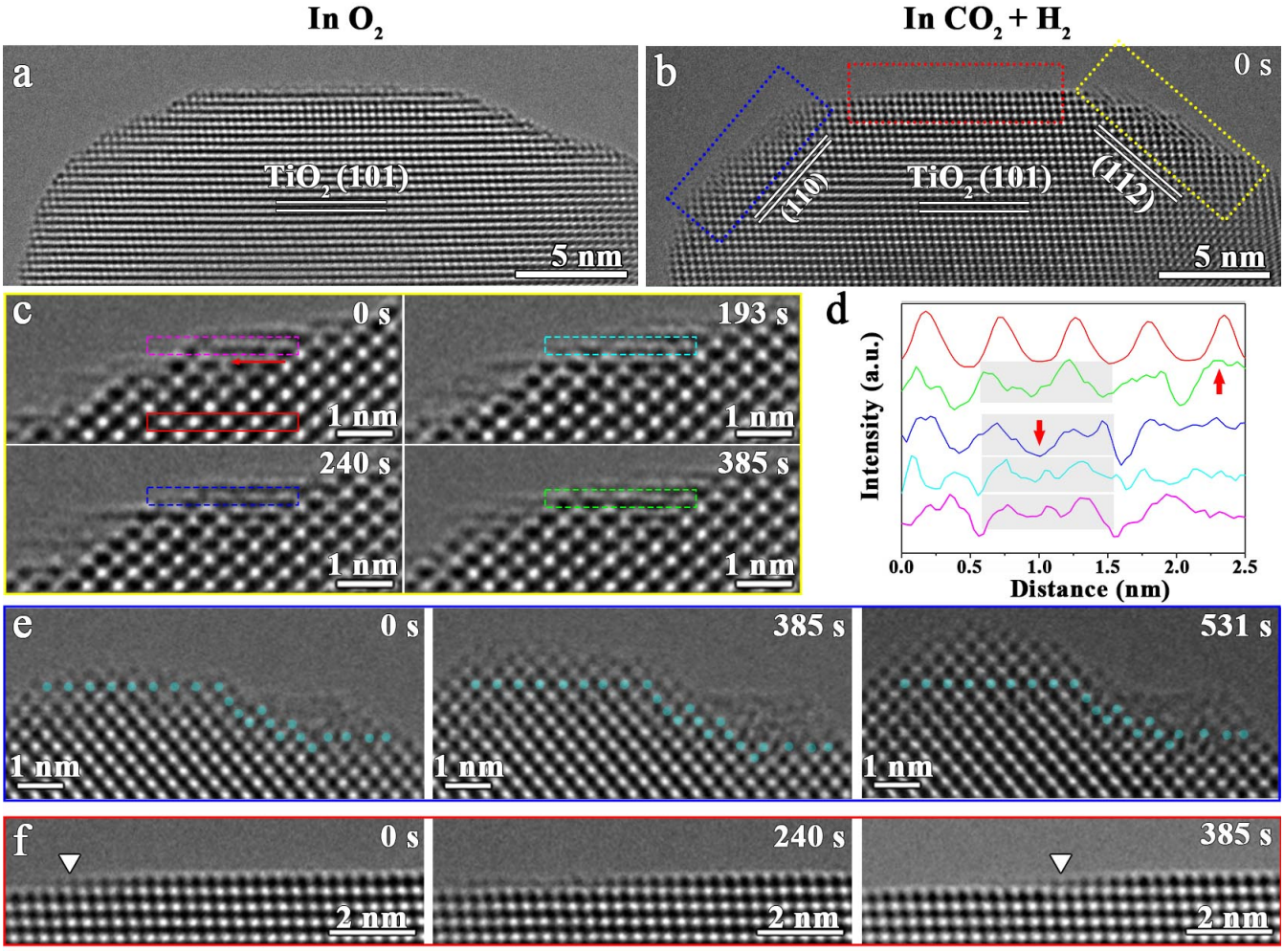

Figure 3. In-situ HRTEM visualization of RWGS reaction dynamics on TiO_2 surfaces under CO_2/H_2 gas flow. (a) HRTEM image of TiO_2 after O_2 pretreatment (4×10^{-3} Torr O_2, 400 °C, 30 min), showing pristine (101), (112), and stepped (110) facets. **b**, TiO_2 exposed to CO_2/H_2 gas mixture (≈ 2×10^{-3} Torr CO_2, ≈ 6×10^{-3} Torr H_2, 500 °C)**,** initiating surface restructuring. **c**, **e**, **f**, Zoom-in views (Supplementary Movie 1) of the dashed regions, capturing RWGS reaction dynamics on the (112) facet (c, d), the stepped (110) facet (e), and the (101) facet (f). In (e), cyan dots mark the atom columns in the initial 0-s image, overlaid onto subsequent snapshots to track atomic rearrangements.

The competitive interplay between reduction (H_2-driven) and oxidation (CO_2-driven) processes on TiO_2 surfaces is critically mediated by O vacancies, with CO_2-driven O replenishment enhanced by O vacancy presence.[23]

To further probe how O vacancies modulate RWGS dynamics, we intentionally introduce O vacancies via H_2 pretreatment (500°C, ~ 6×10^{-3} Torr H_2) and track surface evolution under RWGS conditions by adding 2×10^{-3} Torr CO_2 at 500°C. Figure 4a reveals a pristine TiO_2 structure after O_2 retreatment (~ 4×10^{-3} Torr O_2, 400°C). H_2 exposure induces surface reduction (Fig. 4b), forming a Ti_3O_5 layer on the (101) facet and amorphous regions near the (110) corner due to oxygen loss. Figure 4(c) (zoomed-in view of the dashed blue box in Figure 4(b)) captures oscillatory atomic dynamics on the Ti_3O_5 surface during RWGS, where CO_2 introduction partially restores the TiO_2 surface, as evidenced by the initial absence of significant image contrast on the topmost surface (white arrow in Figure 4(b)) and the recovered lattice fringes in the 230-s HRTEM image (Fig. 4c). Unlike the stoichiometric TiO_2(101) facet (Figure 3(f)), Ti_3O_5 exhibits dynamic evolution, transitioning from the outermost surface to the subsurface. This is evident from regions where atomic resolution is lost and subsequently regained, as marked by purple shading in Figure 4(c). Figure 4(d) provides a detailed view of the amorphous regions identified in Figure 4(b), revealing structural evolution and competing redox processes during the RWGS reaction, similar to untreated TiO_2 in Figure 3(c). Critically, H_2-pretreated TiO_2 exhibits deeper affected zones (Fig. 4(d) vs. Fig. 3(e)), highlighting how preexisting O vacancies generated from the H_2 pretreatment amplify RWGS reaction dynamics.

RWGS reactivity measurements in a plug flow reactor (see more details in experimental session) corroborate the critical role of oxygen vacancies in the reaction mechanisms, as inferred from in-situ TEM observations described above. Both pristine and H_2-pretreated anatase TiO_2 (10% H_2/Ar at 500°C for one hour) exhibit 100% selectivity for CO, achieving steady-state CO_2 conversion rates of ~ 1.2 % and CO production rates of ~ 3×10^{-6} mol/g(TiO_2)/s (Figures 4(e, f)). During thermal ramp-up and stabilization, the catalyst surface undergoes structural reorganization—including increased defect density and surface restructuring—that activates additional sites, while concurrent equilibration of oxygen vacancies and partial Ti reduction under reaction conditions drives the system toward the quasi-steady-state structure with enhanced catalytic activity. The observed RWGS reactivity and the reactivity enhancement from H_2 pretreatment, validated by the repeated measurements (Supplementary Fig. S13), align well with the in situ HRTEM observations presented in Figures 3 and 4, respectively. To bridge the gap between these two approaches, due to the differences in gas pressures and timescale, we have performed ex-situ TEM characterizations of the TiO_2 following both H_2 reduction and CO_2/H_2 reaction treatments in the flow reactor.

These results (see Supplementary Fig. S14) reveal surface restructuring and morphological features indicative of a more reduced state, yet chemically and structurally comparable to those observed in the ETEM experiments, including partial reduction, defect formation, and phase evolution. The relatively limited forward CO production rate is consistent with the in-situ XRD data (Supplementary Fig. S12) and HRTEM observations (Fig. 3),[29] which confirm no bulk structural changes, restricting redox reactivity to surface layers.

The initial reactivity boost in CO_2 conversion (0.65% to 0.85%) and CO production (1.8×10^{-6} to 2.3×10^{-6} mol/g(TiO_2)/s) (Figures 4(e, f), red arrows) during the first 3 h of RWGS aligns with in-situ HRTEM observations (Figs. 4(a-d)). This enhancement stems from H_2 pretreatment-induced O vacancies and Ti_3O_5 formation, which promote CO_2 activation and lead to a transient increase in RWGS activity. However, CO_2 gradually heals these defects via selective O replenishment, driving the system toward a steady state akin to untreated TiO_2 with relatively minor fluctuations (Figures 4(e, f)). The convergence to similar steady-state performance underscores that transient O vacancies—not permanent structural changes—are pivotal for imparting reactivity. This dynamic equilibrium reflects the competition between H_2-driven vacancy generation and CO_2-driven surface passivation (by structural repair), as captured in real-time HRTEM imaging. These findings are corroborated by AP-XPS (Fig. 2f) and TPR measurements (Supplementary Fig. S4), which also indicate surface oxygen depletion upon H_2 exposure. Quantitative analysis of the first TPR peak suggests oxygen removal equivalent to approximately 18 % of a TiO_2(101) monolayer, based on an H_2 uptake of 86 μmol/g and a surface area of 50 m^2/g for anatase TiO_2. This value is comparable to the ~ 8% monolayer intrinsic vacancy concentration reported for rutile TiO_2(110) surfaces.[30] Notably, the observed enhancement in CO production (~ 6 %) on H_2-pretreated TiO_2 correlates well with the extent of oxygen depletion, underscoring the role of surface vacancies in modulating reactivity.

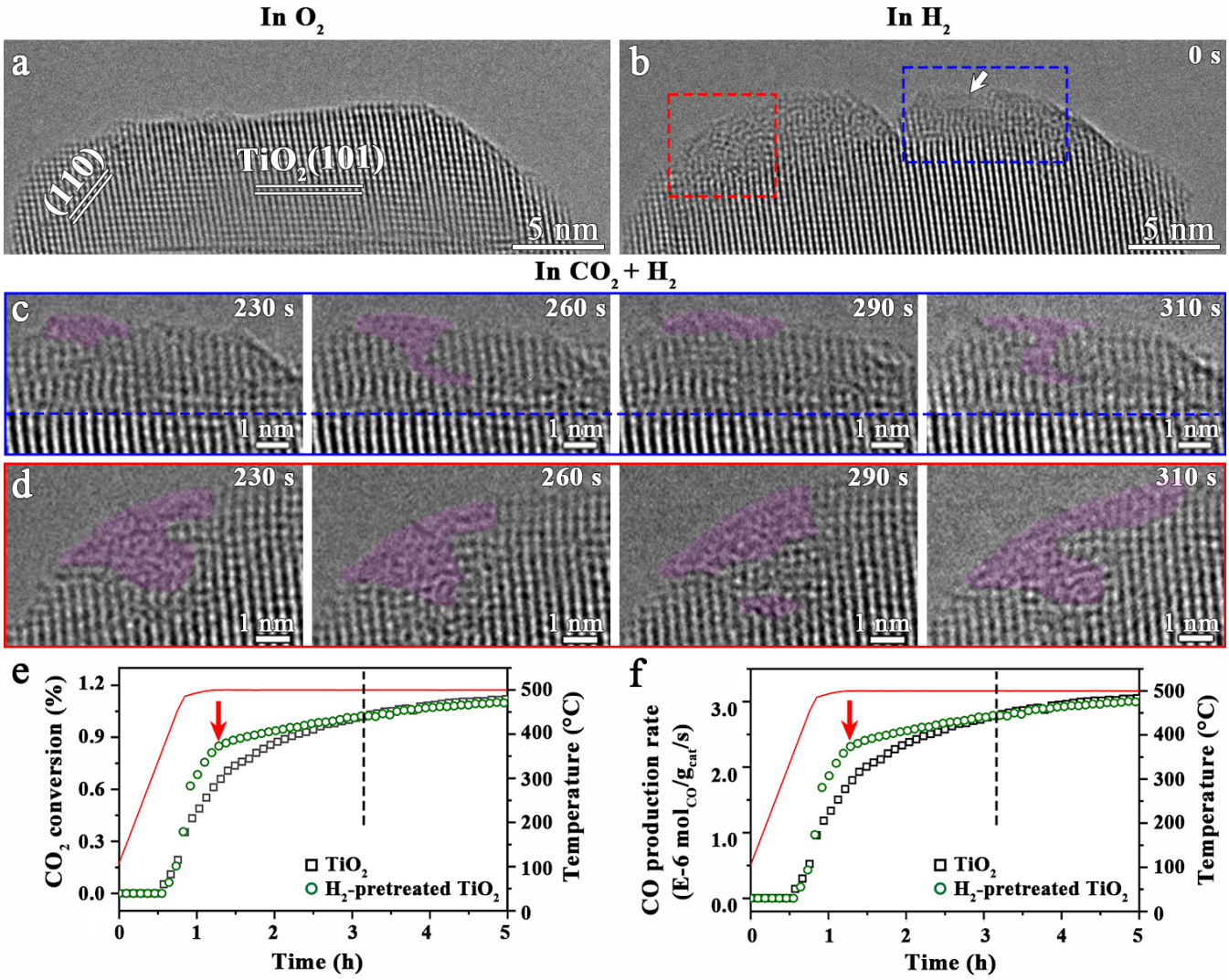

Figure 4. In-situ atomic-scale dynamics of anatase TiO_2 surfaces during H_2 pretreatment and RWGS reactions. **a**, **b**, HRTEM images of anatase TiO_2 under O_2 and then H_2 treatment (500 °C, ~ 6×10^{-3} Torr H_2), respectively. **c**, **d**, In-situ zoomed-in views (Supplementary Movie 2) showing the dynamic evolution of the dashed blue and red box regions (marked in b) of H_2-pretreated TiO_2 during RWGS reaction (500 °C, ~ 2×10^{-3} Torr CO_2, ~ 6×10^{-3} Torr H_2). Purple shading highlights semi-crystalline regions with diminished atomic contrast, reflecting redox-driven structural disorder. **e**, CO_2 conversion profiles for pristine TiO_2 and H_2-pretreated TiO_2 under 1:3 CO_2:H_2 flow (32 sccm), measured during a temperature ramp of 10 °C/min to 500 °C. **f**, Steady-state forward CO production rates (mass-normalized). The red arrows in (**e**, **f**) highlight the point exhibiting the most significant reactivity differences between the pristine TiO_2 and H_2-pretreated TiO_2 samples. The dashed black lines in (**e**, **f**) delineate the consistent long-term trends.

2.3 Mechanistic Insights into Catalytic Reaction Dynamics

To further elucidate the atomic origins of the reaction dynamics on anatase TiO_2 surfaces, we conducted DFT calculations and extensive structural sampling using MLIPs (see more details in Supplementary Figs. S15, S16). Building on training data from our previous work[31], we identify three reductive surface reconstructions phases for the (101) surface, governed by oxygen chemical potential: (i) anatase retention phase ($\Delta\mu_O > -5.26$ eV), preserving bulk-like anatase structure, (ii) shear plane phase ($-5.74 < \Delta\mu_O < -5.26$ eV), featuring off-lattice shear planes, and (iii) highly reduced phase ($\Delta\mu_O < -5.74$ eV), dominated by disordered TiO_3, TiO_4, and TiO_5. Representative atomic structures for each phase are illustrated in Figure 5. In the off-lattice reconstruction (ii), the shear plane is indicated by a dashed line, with atoms outside this boundary deviating from crystalline symmetry, while interior regions retain the crystal order. The highly reduced structure (iii) exhibits a more disordered surface, predominantly composed of TiO_3, TiO_4, and TiO_5 polyhedra, with a smaller fraction of TiO_2 and TiO_6 polyhedra. The O coordination number (CN(O)) is a key descriptor of reduction and reconstruction behaviors. During TiO_2 reduction, O tends to coordinate with an increasing number of Ti atoms, leading to a higher CN(O). The violin plot in Figure 5 presents CN(O) distributions to illustrate surface reorganization. For reference, bulk anatase TiO_2 has an ideal CN(O)=3, while the stoichiometric (101) surface exhibits a slightly lower value of 2.875 due to surface O binding to only two Ti atoms. As reduction progresses, CN(O) increases: the off-lattice shear plane structure has an average CN(O)=3.082, while the highly reduced reconstruction reaches CN(O)=3.566, approaching the CN(O)=3.750 characteristic of bulk Ti_3O_5, consistent with the structural evolution in Figure 1.

For the (112) surface, the stoichiometric surface (iv) features a prominent cavity between line-shaped TiO_5 units, which fills with Ti-O atoms as reduction begins ($\Delta\mu_O \cong -4.79$). The first reduced structure (v) stabilizes within the range $-5.56 < \Delta\mu_O < -4.79$ eV, forming a highly symmetric 1T structure with P3m1 symmetry in its outermost layer. At $\Delta\mu_O$ below -5.56 eV, the structure undergoes a transition into a highly disordered, amorphous-like structure, as depicted in Figure 5 (vi). Similar to the (101) surfaces, the CN(O) increases during the reduction process. The stoichiometric (112) surface initially has a CN(O) of 2.750, which rises to 2.972 in the 1T-like reduced structure (v) and further to 3.600 in the highly reduced reconstruction (vi).

Compared to the (101) surface, reduction on the (112) surface initiates at a significantly higher $\Delta\mu_O$—approximately 0.5 eV higher. This behavior indicates that the (112) surface is more prone to reduction than the most stable (101) surface, consistent with the in-situ HRTEM observations in Fig. 3, suggesting the reactivity differences among various surface facets. It is important to note that in theoretical calculations, the oxygen chemical potential for a given surface free energy or reconstructed structure is typically treated as a constant value. However, real catalytic reactions involve both forward and reverse processes due to the presence of mixed gas environments, leading to complex surface and interfacial dynamics. As shown in Figs. 3 and 4, the evolution of surface structures includes oscillatory atomic-scale dynamics, emphasizing the interplay between competing oxidation and reduction reactions. These phenomena are further modulated by varying surface coordination conditions, which exhibit distinct reactivities toward gas-solid interfacial reactions involving adsorption and dissociation processes. The observed differences in potential transitions between pristine and reduced TiO_2 surfaces under identical reaction conditions highlight the variability in surface reactivity, driven by structural and electronic property variations.

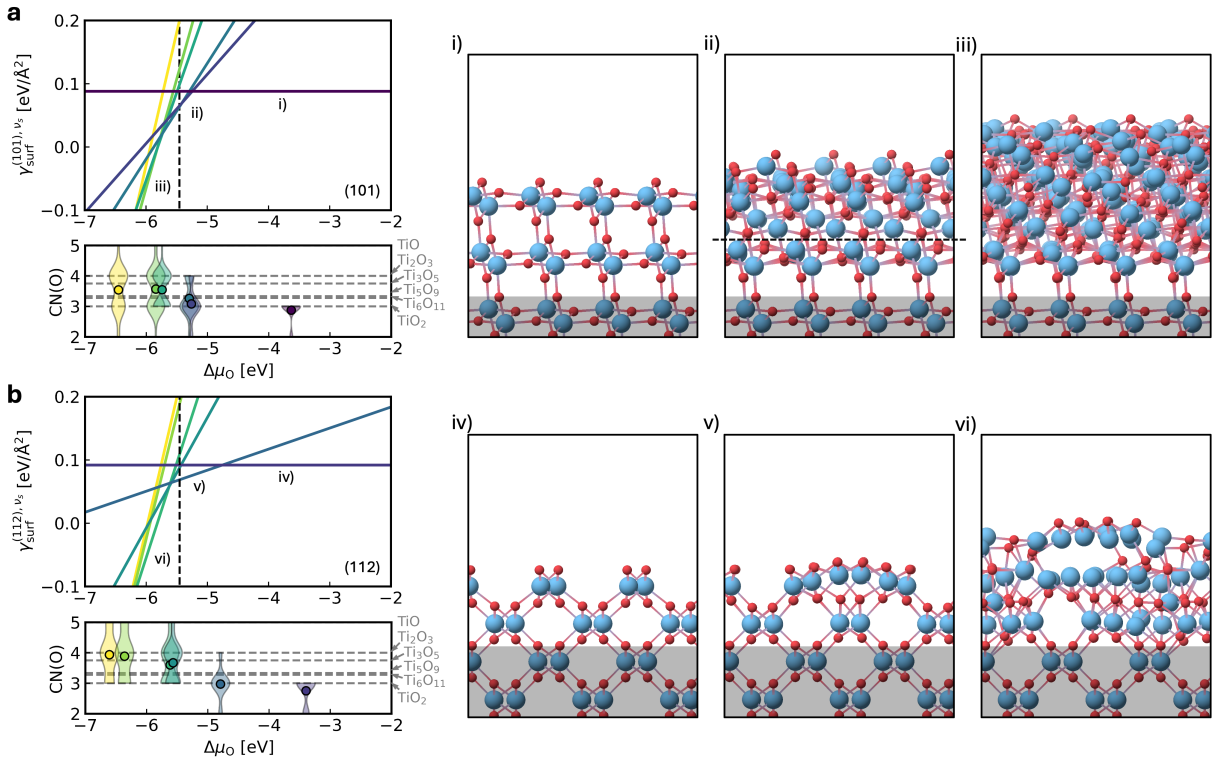

Figure 5. DFT-calculated surface free energies ($\gamma_{\mathrm{surf}}^{(hkl),\nu_s}$) as a function of O chemical potential ($\Delta\mu_O$) for anatase **a**, (101) and **b**, (112) surfaces. The lowest-energy structures, identified through MLIP-assisted grand canonical samplings, were further

optimized via DFT and are represented by colored solid lines. The vertical dashed line indicates the O-poor limit ($\Delta\mu_O = -5.47$ eV), corresponding to the formation energy of bulk anatase TiO_2 (per O atom). Violin plots below the phase diagrams illustrate the coordination numbers of O (CN(O)) in the surface region, with average CN(O) values shown as circles. Horizontal gray dashed lines denote average CN(O) values for bulk Ti-O phases. Representative atomic structures are displayed in the right panel, where Ti and O atoms are depicted as large cyan and small red spheres, respectively. The fixed bulk region is shaded in gray, distinguishing it from the surface region.

To gain deeper insight into these dynamics, we performed electronic structure analysis of the pristine and reduced TiO_2(101) surfaces, focusing on the binding characteristics of H and CO_2. Figure 6(a) presents the Bader charge distribution of Ti atoms on both surfaces. On the pristine surface, the average charge of surface Ti atoms is +2.34, closely matching the bulk Ti charge of +2.49, with a small standard deviation of 0.025. Despite the presence of five-fold-coordinated surface Ti sites, their oxidation state remains largely unaltered. However, on the reduced surface, Ti atoms undergo a significant reduction in charge, with an average Ti charge of +1.55 and a much larger standard deviation of 0.355, indicating substantial local charge redistribution upon surface reduction.

This phenomenon is clearly reflected in the spin-resolved partial density-of-states (PDOS) shown in Figure 6(b). The pristine structure exhibits a well-defined band gap with no defect states, leading to a symmetric occupation of spin components. In contrast, the reduced surface shows the emergence of significant mid-gap states that are spin-polarized and predominantly localized in the up-spin channel. This spin anisotropy in the filled mid-gap defect states, primarily derived from Ti 3*d* orbitals, indicates the formation of Ti^{3+} polarons at the surface. On the other hand, mid-gap contributions from oxygen 2*p* states are nearly negligible, and the occupied O 2*p* states below the Fermi level remain relatively symmetric between spin channels. This suggests that hole localization on oxygen sites (O^- polarons) is not significant, as no unoccupied spin-polarized states characteristic of hole polarons are observed near the valence band edge. The high concentration of Ti^{3+} polarons at the reduced surface implies distinct adsorption characteristics for adsorbates compared to the pristine surface.

We then computed the binding energies of H and CO_2 on both pristine and reduced TiO_2(101) surfaces. To systematically explore all possible adsorption sites, we employed a graph-based approach to generate symmetry-

inequivalent, unique initial adsorption configurations, ensuring a comprehensive search for the most favorable binding sites and energies. Interestingly, both H and CO_2 exhibit stronger binding on the reduced TiO_2(101), with binding energies of -5.581 and -6.671 eV, respectively. In contrast, their adsorption on the pristine surface is much weaker, with binding energies of -0.243 and -0.736 eV, respectively. More specifically, H preferentially binds at the two-fold bridge oxygen site on the pristine surface but relocates to the Ti-Ti bridge site on the reduced surface. Meanwhile, the CO_2 molecule is weakly physiosorbed at the five-fold Ti site on the pristine surface, with a bond length of 2.47 Å. In contrast, on the reduced surface, CO_2 adopts a bent configuration, with both oxygen atoms binding to adjacent Ti atoms at atop sites. This bent geometry suggests activation of CO_2, facilitating its dissociation and enhancing its surface reactivity.[32]

To elucidate the nature of adsorption interactions, we performed Crystal Orbital Hamilton Population (-COHP) analysis for H and CO_2 on both pristine and reduced surfaces. This analysis provides insight into the bonding characteristics by identifying bonding and antibonding states relative to the Fermi energy. As discussed above, H binds at the bridge O site on the pristine surface, with its bonding state located at approximately -8 eV below the Fermi level. Notably, no bonding states appear near the Fermi energy (-5 to 0 eV), indicating that the interaction is deeply localized within the valence band rather than contributing to surface reactivity. The integrated COHP (iCOHP) values for spin-up and spin-down components are highly negative (-3.969 and -3.968, respectively), suggesting a strongly covalent bonding interaction. However, despite this strong local bond formation, the overall binding energy remains weak (-0.243 eV), indicating that H adsorption is not well stabilized on the pristine surface. This discrepancy suggests that while H forms a local covalent bond with O, other factors, such as lack of charge transfer, prevent strong overall adsorption.

In contrast, CO_2 binds weakly at the Ti atop site, with no distinct bonding or antibonding states near the Fermi level. The very small iCOHP values (-0.446 for both spin-up and spin-down) indicate that the interaction is neither covalent nor ionic but instead dominated by weak van der Waals forces, consistent with its physisorption behavior. On the reduced surface, distinct changes in the electronic structure emerge. For H adsorption, a clear bonding state appears closer to the Fermi level, around -4 eV, suggesting increased interaction with the surface. However, the iCOHP values (-1.546 for spin-up and -1.621 for spin-down) are less negative than those on the

pristine surface, despite the much stronger binding energy (-5.581 eV). This suggests that H binding on the reduced surface has a more ionic character, likely influenced by charge redistribution and stronger electrostatic interactions with reduced Ti sites.

For CO_2 adsorption, a strong bonding state emerges at -2 eV, significantly different from the weak physisorption observed on the pristine surface. The highly negative iCOHP values (-4.033 for spin-up and -4.162 for spin-down) indicate that CO_2 interacts via a strong covalent bond rather than simple electrostatic attraction, consistent with its bent adsorption configuration. These findings reveal a fundamental shift in adsorption behavior upon surface reduction. While the pristine surface exhibits weak overall hydrogen binding despite strong localized H-O covalent interactions, the reduced surface promotes significantly stronger, more ionic hydrogen adsorption and enhanced covalent CO_2 binding. This change is crucial for CO_2 activation and dissociation, providing insight into the reduction and reoxidation processes occurring under different reaction conditions. The notably stronger binding of H on the reduced surface suggests that once an initial reduction occurs, the surface becomes highly favorable for further hydrogen adsorption. This autocatalytic reduction process explains why TiO_2 readily reduces in pure H_2 environments—once some oxygen vacancies form through the oxidation of adsorbed hydrogen, they serve as high-affinity sites for further H adsorption, accelerating continued reduction.[33] In contrast, pristine TiO_2 does not strongly bind H, making reduction a slow process until a sufficient number of vacancies accumulate to trigger autocatalysis.

Under RWGS conditions, exposure to CO_2 leads to the exceptionally strong adsorption of CO_2 on the reduced TiO_2 surface. This occurs due to the high concentration of O vacancies and Ti^{3+} centers, which enhance electron transfer to CO_2, promoting its dissociation and supplying oxygen atoms to refill vacancies. This process effectively re-oxidizes Ti^{3+} back to Ti^{4+}, restoring the pristine TiO_2 phase. Since reoxidation eliminates high-affinity sites for H adsorption, the system undergoes a self-sustaining transition from reduced to pristine TiO_2, preventing further reduction despite the continued presence of H_2. These binding energy trends align well with experimental observations. Under pure H_2 conditions, the weak initial interaction of H with pristine TiO_2 allows reduction to proceed gradually, eventually leading to a fully reduced TiO_2 surface. However, under RWGS conditions, the strong affinity of CO_2 for reduced TiO_2 drives its dissociation, leading to reoxidation and the restoration of a pristine-like phase, as shown in the reactivity trends in Figure 4(e, f). This interplay between adsorption-driven reduction and

reoxidation creates a dynamic surface state, where TiO_2 continuously cycles between reduced and oxidized phases depending on the prevailing reaction environment.

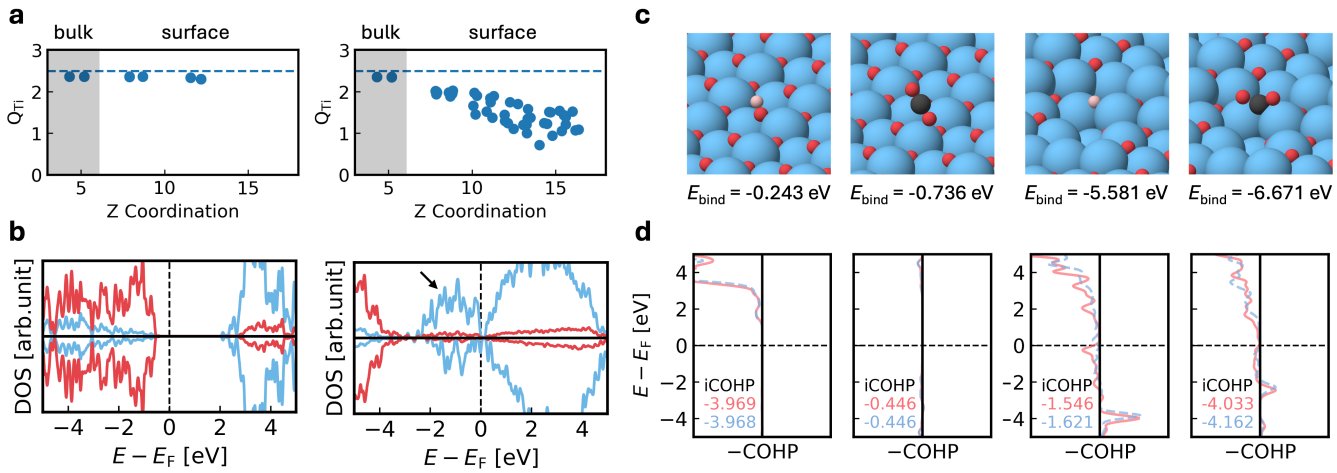

Figure 6. Electronic structure analyses for pristine and reduced TiO_2(101) surfaces. **a**, Bader charge (Q_{Ti}) of Ti atoms, plotted against their z-coordinates in the supercell for the pristine (left) and reduced (right) surfaces. The horizontal dashed line indicates the reference Bader charge of Ti in bulk anatase TiO_2. **b**, Spin-resolved partial density-of-states (PDOS) for the pristine (left) and reduced (right) surfaces. Ti 3*d* and O 2*p* states are shown in blue and red lines, respectively. The arrow indicates the defect states associated with Ti^{3+} within the band gap of the reduced surface. **c**, Adsorption configurations of H and CO_2 on pristine (left) and reduced (right) TiO_2(101), with binding energies (E_{bind}) noted below each panel. Ti, O, C, and H atoms are represented by blue, red, black, and white spheres, respectively. **d**, Crystal Orbital Hamilton Population (-COHP) analysis for the bonding interactions between each adsorbate and its neighboring surface atoms. Spin-up and spin-down components are represented as red solid and blue dashed lines, respectively. Positive peaks indicate bonding states, whereas negative values correspond to antibonding interactions. Integrated COHP (iCOHP) values are provided as insets.

The results presented above resolve the atomic-scale redox mechanisms governing the RWGS reaction on anatase TiO_2, establishing O vacancy dynamics and surface orientation as pivotal factors. The facet-dependent activity arises from the preferential reduction of undercoordinated sites on high-index (112) and stepped surfaces, where H_2 generates O vacancies and Ti^{3+}-rich surface layers while the dominant (101) facet remains inert. The apparent discrepancy in dynamic behaviors of the (101) facet arises from differences in reaction environments: under H_2 alone (Figs. 1 and 4), the (101) surface undergoes reduction via lattice oxygen loss, forming Ti_3O_5 due to

favorable thermodynamics. In contrast, during CO_2 + H_2 catalysis (Fig. 3), competing reduction and reoxidation processes dominate. CO_2 acts as a dynamic oxidant, replenishing lattice oxygen and stabilizing partially reduced regions—particularly on the more stable (101) facet, as supported by DFT (Fig. 5). Consequently, while the (101) facet is reducible under strongly reducing conditions, it remains relatively stable during RWGS, whereas the more reducible (112) surface undergoes greater restructuring driven by redox cycling.

CO_2 rapidly heals the O vacancies—threefold faster than H_2-induced reduction—restoring lattice O and suppressing sustained catalytic activity. This competition creates oscillatory atomic-scale dynamics but limits overall reactivity due to the dominance of inert (101) facets and CO_2-driven passivation of active sites. Mechanistically, these findings define anatase TiO_2 as a dynamic equilibrium between defect creation and annihilation, governed by local coordination environments. Practically, pure anatase TiO_2 is generally not an effec tive catalyst for the RWGS reaction due to its limited ability to activate CO_2 and dissociate H_2 (Figs. 4(e, f)). How ever, when used as an oxide support for dispersed metal species—such as single atoms or nanoparticles—TiO_2 ca n enable significantly enhanced catalytic performance.[6,7,21,22,34] These metal–support systems exhibit strong interfa cial interactions that promote key steps in the RWGS reaction, including hydrogen activation and CO_2 reduction. I mportantly, structure–reactivity studies have revealed that the catalytic activity and stability are highly sensitive to the crystallographic facets of the TiO_2 support.[21,22,34,35] Specific surface orientations can stabilize different metal c onfigurations or defect structures, which in turn modulate the reaction pathway. The work highlights surface engineering as a critical lever for optimization: selectively exposing reactive facets (e.g., (112), (110)) or stabilizing O vacancies (via doping, strain, or heterostructuring) could amplify RWGS efficiency of TiO_2 support. Such strategies could transform TiO_2 into a tunable platform for heterogeneous catalyst development for CO_2 conversion, bridging atomic-scale defect control to industrial-scale sustainability goals like carbon-neutral fuel synthesis. By linking surface geometry, defect lifetimes, and reaction kinetics, this work provides a framework for designing adaptive oxide tailored for dynamic gas-solid interfaces.

Conclusions

This study provides direct evidence of the dynamic interplay of O vacancy generation and replenishment in governing the RGWS reaction on anatase TiO_2 surfaces. Through in-situ atomic-scale imaging and computational modeling, we demonstrate that RWGS proceeds via redox cycle mediated by surface orientation and defect dynamics: (i) reduction-driven O loss: H_2 preferentially reduces undercoordinated sites on high-indexed (112) and stepped surfaces, forming O vacancies and Ti^{3+}-rich domains, while the thermodynamically stable (101) facet remains structurally intact and inert. (ii) oxidation-driven O replenishment: CO_2 dissociates at O vacancy sites, restoring lattice O with kinetics approximately three times faster than reduction. This rapid healing passivates active sites, leading to transient activity loss. The competition between these processes drives oscillatory atomic-scale dynamics, yet results in modest overall reactivity due to two key factors: (i) CO_2-induced healing of O vacancies, which suppresses sustained catalytic activity, and (ii) the dominance of inert (101) facets on anatase TiO_2 NPs. These results underscore the critical role of atomic-scale defect control and facet engineering in tailoring oxide catalysts for sustainable CO_2 conversion technologies.

Experimental methods

In-situ environmental TEM experiments. The anatase TiO_2 nanoparticles (99.9% anatase, average particle diameter ~ 30 nm) were purchased from Research Nanomaterials Inc. and subsequently loaded onto through-hole SiN_x thin films on DENSsolutions chips. In-situ TEM experiments were performed using a single-tilt DENSsolutions heating holder within an environmental TEM (FEI Titan 80-300) equipped with an objective-lens aberration corrector and a differential pumping system. The annealing processes were conducted at a heating rate of 100 °C/min. EELS measurements were performed in the ETEM using probe scanning mode following in-situ treatments under various gas environments. To thoroughly evaluate the effects of the electron beam, comparative experiments were performed to assess RWGS reaction dynamics and EELS spectrum acquisition process of TiO_2 under electron beam blanked conditions (Fig. S10). Additionally, we investigated the effects of vacuum annealing and continuous electron beam irradiation on TiO_2 reduction and found that these effects were less pronounced than those observed in H_2 (Fig. S11).

AP-XPS measurements. AP-XPS experiments were conducted at the Center for Functional Nanomaterials, Brookhaven National Laboratory. The system utilized a SPECS Phoibos 100 MCD analyzer for XPS measurements, coupled with a monochromatic Al Kα X-ray source (1486.6 eV, ~ 0.25 eV line width), focused to a spot size smaller than 300 μm. To minimize charging effects in the AP-XPS measurements, the conductivity of the sample was improved by pressing a small amount of anatase TiO_2 powders onto a Tantalum (Ta) foil. The Ta foil was subsequently spot welded directly onto the sample holder, which was heated using a laser heater positioned at the backside of the sample holder. The AP-XPS setup, equipped with multiple differential pumping apertures, enables gas pressures in the Torr range near the sample while maintaining ultrahigh vacuum (UHV) conditions in the hemispherical analyzer. All spectra were acquired at a 20° takeoff angle relative to the electron analyzer optics.

In-situ XRD measurements. X-ray diffraction experiment was performed at beamline BL2-1 at Stanford Synchrotron Radiation Lightsource at SLAC National Accelerator Laboratory using X-ray energy of 17 keV (0.72932 A). 2.7 mg of pressed and sieved anatase TiO_2 is packed in a 1 mm capillary on a flow cell reactor. The sample was first pretreated in 20% O_2 in He for a half hour. After cooling and purging the cell with helium, the

sample was then exposed to a reaction mixture (24: 8 sccm H_2: CO_2) and heated from 200 °C to 700 °C, with a 30-minute dwell at every 50 °C increment, then from 700 °C to 720 °C with a 20-minute dwell at every 10 °C increment.

Physical adsorption measurements. The surface area of the as-received anatase TiO_2 was measured by physical adsorption at 77 K with nitrogen as the adsorbent gas on a Micromeritics 3Flex. The quantity of N_2 adsorption over relative pressure (P/P_0) range of 0.05–0.35 was used to calculate the BET surface area. A carbon black surface area reference material (Micromeritics part # 004-16833-00) with a reported multi-point surface area of 21.5±0.8 m^2/g was run simultaneously to ensure the accuracy of the measured surface area of the as-received anatase TiO_2 support.

RWGS reactivity measurements. Reactivity measurements were conducted in a packed-bed flow reactor using a 3/8-inch outer diameter stainless steel tube coated with an inert Silcolloy® coating. The reactor tube was heated within a copper block furnace using 5-inch resistive cartridge heaters, and the temperature was monitored by a K-type thermocouple positioned in the catalyst bed. Anatase TiO_2 samples (20 mg, US research Nanomaterials Inc, 30 nm) were diluted with SiO_2 (500 mg, Sigma Aldrich, 40–150 mesh, 90–425 μm particle size) and thoroughly mixed using a vortex mixer to prevent the formation of hotspots. The diluted catalyst mixture was loaded into the inert stainless steel reactor tube and positioned between two plugs of quartz wool. The catalyst was pretreated in 100% O_2 at 400°C for 30 minutes, with a ramp rate of 10°C/min, and then cooled to room temperature under an O_2 atmosphere. For the H_2-pretreated TiO_2 catalysts, an additional treatment with 10% H_2/Ar at 500°C for one hour was performed after the O_2 pretreatment. The reactor was then purged with Ar to remove residual pretreated gas. A reactant mixture (32 sccm with a 1: 3 CO_2: H_2 ratio) was introduced at room temperature and ramped to 500 °C over one 1 hour, where it was maintained for 15 hours to conduct the reaction study. The product gases were analyzed using gas chromatograph (SRI 8610C) with a methanizer-equipped flame ionizing detector and thermal conductivity detector.

Density functional theory calculations. Spin-polarized density functional theory (DFT) calculations were carried out using the projector-augmented wave (PAW) method[36] within the Vienna Ab initio Simulation Package (VASP).[37,38] The valence states explicitly included the 3*p*, 3*d*, and 4*s* orbitals of Ti, along with the 2*s* and 2*p* orbitals

of O. The electronic exchange and correlation were modeled using the semi-local generalized gradient approximation (GGA) with the Perdew-Burke-Ernzerhof (PBE) functional,[39] enhanced by van der Waals (vdW) corrections following the Tkatchenko-Scheffler (TS) scheme.[40] To accurately describe the electronic structure of TiO_2, an on-site Coulomb interaction correction (DFT+U) was applied to the Ti 3d electrons using the Dudarev approach,[41] with the effective Hubbard parameter of 3.5 eV.[42,43] The calculations employed a plane-wave basis set with a kinetic energy cutoff of 500 eV. Brillouin zone sampling was performed with a reciprocal distance of 0.03 $Å^{-1}$. The lattice parameters were optimized by iteratively minimizing lattice stress and atomic displacements until the external pressure fell below 0.5 kbar. Convergence criteria were defined as total energy changes below 10^{-5} eV and 10^{-4} eV for electronic and ionic relaxations, respectively. Under these conditions, the atomic forces in the optimized bulk TiO_2 structure were minimized to less than 0.01 eV/Å. The aforementioned DFT setups are consistent with Ref [26] to ensure the continuous use of the data for further training of the machine-learning potentials.

Surface calculations utilized supercell geometries with periodic boundary conditions, incorporating a vacuum gap of at least 20 Å to eliminate unintended interactions between repeating images. For the TiO_2(101) (TiO_2(112)) surface, asymmetric slab models were designed using (3×1) ((2×1)) surface unit cells, comprising a minimum of 24 (12) atomic layers, with the bottom 12 (6) layers fixed at their bulk positions. The energies used in the DFT surface phase diagrams were computed with a dipole correction applied perpendicular to the surface to counteract artificial electrostatic effects. However, no dipole correction was included in the DFT results used for training the machine-learning potentials to prevent inaccuracies arising from artificial energy modifications.

MACE architecture. The MLIP model was implemented using the MACE architecture, an equivariant message-passing graph tensor network designed to encode many-body atomic geometry information at each layer.[44] The initial training set for the TiO_2 system was obtained from the database provided in Ref [26]. This training set includes rutile and anatase TiO_2 surfaces mostly for rutile (110) and anatase (101). In the MACE model used herein, two message-passing layers were utilized, with spherical expansions up to l_{max} = 3, and 4-body messages were incorporated in each layer, corresponding to a correlation order of 3. All models were constructed with a 128-channel dimension for tensor decomposition. A radial cutoff of 6 Å was applied, and the interatomic distances were

expanded into 8 Bessel functions, which were further multiplied by a smooth polynomial cutoff function to generate the radial features. The model adopted maximal message equivariance with an order of $L = 1$. For better accuracy and expandability, fine-tuning the medium materials project[45] foundation model (MACE-MP-0[46]) was used.

Grand canonical genetic algorithm. To investigate the chemical space of anatase TiO_2 surfaces under reductive conditions, we employed a global optimization strategy using the grand canonical genetic algorithm (GCGA), which was implemented in our proprietary GOCIA package.[47] In this framework, the system is treated as a grand canonical ensemble where Ti and O adsorbates interact with the anatase slab, aiming to minimize the coverage-dependent grand canonical free energy Ω, which is expressed as:

$$\Omega = U - TS - \sum_i n_i \mu_i = G_{\text{surf}}^{(110),\nu_s} - G_{\text{surf}}^{(110),\nu_0} - \Delta n_{\text{Ti}} \mu_{\text{Ti}} - \Delta n_{\text{O}} \mu_{\text{O}},$$

Here, $G_{\text{surf}}^{(110),\nu_s}$ and $G_{\text{surf}}^{(110),\nu_0}$ correspond to the Gibbs free energies of the newly generated (termination ν_s) and reference (termination ν_0) TiO_2 slabs, respectively. The variables n_i and μ_i denote the number of atoms of species i in the periodic system and their respective chemical potentials. The chemical potentials of Ti and O (μ_{Ti} and μ_{O}) are constrained by the equilibrium with bulk anatase TiO_2, satisfying the relation: $g_{\text{TiO}_2,\text{bulk}} = \mu_{\text{Ti}} + 2\mu_{\text{O}}$. Additionally, μ_{O} is determined by the equilibrium with an oxygen gas-phase reservoir: $\mu_{\text{O}} = \frac{1}{2} E_{\text{O}_2} + \Delta\mu_{\text{O}}$, where E_{O_2} represents the total energy of an isolated O_2 molecule, incorporating zero-point energy (ZPE) corrections.[48]

For GCGA sampling, a population of 30 structures and a mutation rate of 40% were chosen. The initial set of candidates was generated using the bond length distribution algorithm (BLDA), which randomly constructs structures based on covalent radii.[49] A pre-optimization step utilizing Hookean potentials was applied to ensure physically reasonable initial geometries before local optimization with MLIP and energy evaluation. The generation of offspring followed a split-and-splice approach,[50] in which parent slabs were sectioned along random planes and then recombined.

Each candidate was assigned a fitness score based on mating frequency and grand canonical free energy, prioritizing structures with lower free energy and infrequent mating for further evolution. A similarity check was implemented to prevent duplicate structures from being added to the population. Mutation operations included the

addition or removal of adsorbates, random displacement of surface atoms, translation of the buffer slab along the x- or y-axis by 1/n (where n = 2, 3, 6) of the cell length, and permutation of half of the buffer region. If offspring exhibited excessive similarity to their parents, their mutation rate was increased to 100%. To maintain a constant population size, the candidate with the lowest fitness was achieved after each addition.

Ab initio thermodynamics. To evaluate the stability of different reconstructed terminations of the anatase TiO_2 surface, we employed an ab initio thermodynamics approach.[51] Similar to the grand canonical free energy approach discussed earlier, the surfaces were assumed to be in thermodynamic equilibrium with an oxygen-containing gas phase. This allowed for the computation of the surface free energy, $\gamma_{\mathrm{surf}}^{(hkl),\nu_s}$, as follows:

$$\gamma_{\mathrm{surf}}^{(hkl),\nu_s} = \frac{1}{A^{(hkl)}}\left[G_{\mathrm{surf}}^{(hkl),\nu_s} - \sum_i n_i\mu_i\right]$$

Here, the Gibbs free energies of the condensed phases were approximated using DFT-derived total energies,[52] enabling the equation to be rewritten as:

$$\gamma_{\mathrm{surf}}^{(hkl),\nu_s}(\Delta\mu_{\mathrm{O}}) = \frac{1}{A^{(hkl)}}\left[E_{\mathrm{surf}}^{(hkl),\nu_s} - n_{\mathrm{Ti}}E_{\mathrm{TiO_2,bulk}} - (n_{\mathrm{O}} - 2n_{\mathrm{Ti}})\left(\frac{1}{2}E_{\mathrm{O_2}} + \Delta\mu_{\mathrm{O}}\right)\right].$$

This formulation provides a direct means of assessing the thermodynamic stability of various surface configurations under different environmental conditions.

SUPPORTING INFORMATION

Supporting information is available free of charge on the ACS publication website:

Supplementary figures, and Supplementary in-situ TEM movies

AUTHOR INFORMATION

Corresponding Author

***E-mail**: jyang1@bnl.gov

Notes

The authors declare no competing interests.

ACKNOWLEDGMENT

The work was supported by the Division of Chemical Sciences, Geosciences, and Biosciences, Office of Basic Energy Sciences, U.S. Department of Energy (DOE) as part of the Accelerate Innovations in Emerging Technologies initiative FWP 101064. The work at SUNY Binghamton was supported by the DOE, Office of Basic Energy Sciences, Division of Materials Sciences and Engineering under Award No. DE-SC0001135. This research used electron microscopies and ambient-pressure X-ray photoelectron spectroscopy of the Center for Functional Nanomaterials, at Brookhaven National Laboratory, which is supported by the US Department of Energy, Office of Basic Energy Sciences, under Contract No. DE-SC0012704. Use of the Stanford Synchrotron Radiation Lightsource, SLAC National Accelerator Laboratory, is supported by the U.S. Department of Energy, Office of Science, Office of Basic Energy Sciences under Contract No. DE-AC02-76SF00515.

References

(1) Yoon, B. S.; Yu, Y. J.; Park, G.-J.; Choi, S.-B.; Kim, S.-J.; Ko, C. H. Preparation and Optimization of Eggshell-Type Cu/Zn/Al_2O_3 Pellet Catalysts for Methanol Reforming. *Catal. Today* **2024**, *425*, 114353.

(2) Matte, L. P.; Kilian, A. S.; Luza, L.; Alves, M. C. M.; Morais, J.; Baptista, D. L.; Dupont, J.; Bernardi, F. Influence of the CeO_2 Support on the Reduction Properties of Cu/CeO_2 and Ni/CeO_2 Nanoparticles. *J. Phys. Chem. C* **2015**, *119* (47), 26459–26470.

(3) Xu, W.; Liu, Z.; Johnston-Peck, A. C.; Senanayake, S. D.; Zhou, G.; Stacchiola, D.; Stach, E. A.; Rodriguez, J. A. Steam Reforming of Ethanol on Ni/CeO_2: Reaction Pathway and Interaction between Ni and the CeO_2 Support. *Acs Catal.* **2013**, *3* (5), 975–984.

(4) Yu, J.; Qin, X.; Yang, Y.; Lv, M.; Yin, P.; Wang, L.; Ren, Z.; Song, B.; Li, Q.; Zheng, L. Highly Stable Pt/CeO_2 Catalyst with Embedding Structure toward Water–Gas Shift Reaction. *J. Am. Chem. Soc.* **2023**, *146* (1), 1071–1080.

(5) Zhao, Z.; Wang, M.; Ma, P.; Zheng, Y.; Chen, J.; Li, H.; Zhang, X.; Zheng, K.; Kuang, Q.; Xie, Z.-X. Atomically Dispersed Pt/CeO_2 Catalyst with Superior CO Selectivity in Reverse Water Gas Shift Reaction. *Appl. Catal. B Environ.* **2021**, *291*, 120101.

(6) Zhou, R.; Rui, N.; Fan, Z.; Liu, C. Effect of the Structure of Ni/TiO_2 Catalyst on CO_2 Methanation. *Int. J. Hydrogen Energy* **2016**, *41* (47), 22017–22025.

(7) Messou, D.; Bernardin, V.; Meunier, F.; Ordoño, M. B.; Urakawa, A.; Machado, B. F.; Collière, V.; Philippe, R.; Serp, P.; Le Berre, C. Origin of the Synergistic Effect between TiO_2 Crystalline Phases in the Ni/TiO_2-Catalyzed CO_2 Methanation Reaction. *J. Catal.* **2021**, *398*, 14–28.

(8) Chen, W.-T.; Chan, A.; Sun-Waterhouse, D.; Llorca, J.; Idriss, H.; Waterhouse, G. I. N. Performance Comparison of Ni/TiO_2 and Au/TiO_2 Photocatalysts for H_2 Production in Different Alcohol-Water Mixtures. *J. Catal.* **2018**, *367*, 27–42.

(9) Yang, Y.; Liu, J.; Liu, F.; Wu, D. Reaction Mechanism of CO_2 Methanation over Rh/TiO_2 Catalyst. *Fuel* **2020**, *276*, 118093.

(10) Karelovic, A.; Ruiz, P. Mechanistic Study of Low Temperature CO_2 Methanation over Rh/TiO_2 Catalysts. *J. Catal.* **2013**, *301*, 141–153.

(11) Frey, H.; Beck, A.; Huang, X.; van Bokhoven, J. A.; Willinger, M.-G. Dynamic Interplay between Metal Nanoparticles and Oxide Support under Redox Conditions. *Science* **2022**, *376* (6596), 982–987.

(12) He, Y.; Liu, J.-C.; Luo, L.; Wang, Y.-G.; Zhu, J.; Du, Y.; Li, J.; Mao, S. X.; Wang, C. Size-Dependent Dynamic Structures of Supported Gold Nanoparticles in CO Oxidation Reaction Condition. *Proc. Natl. Acad. Sci.* **2018**, *115* (30), 7700–7705.

(13) Du, X.; Huang, Y.; Pan, X.; Han, B.; Su, Y.; Jiang, Q.; Li, M.; Tang, H.; Li, G.; Qiao, B. Size-Dependent Strong Metal-Support Interaction in TiO_2 Supported Au Nanocatalysts. *Nat. Commun.* **2020**, *11*, 5811.

(14) Liu, Z.; Huang, E.; Orozco, I.; Liao, W.; Palomino, R. M.; Rui, N.; Duchoň, T.; Nemšák, S.; Grinter, D. C.; Mahapatra, M. Water-Promoted Interfacial Pathways in Methane Oxidation to Methanol on a CeO_2-Cu_2O Catalyst. *Science* **2020**, *368* (6490), 513–517.

(15) Huang, E.; Orozco, I.; Ramírez, P. J.; Liu, Z.; Zhang, F.; Mahapatra, M.; Nemsak, S.; Senanayake, S. D.; Rodriguez, J. A.; Liu, P. Selective Methane Oxidation to Methanol on ZnO/Cu_2O/Cu (111) Catalysts: Multiple Site-Dependent Behaviors. *J. Am. Chem. Soc.* **2021**, *143* (45), 19018–19032.

(16) Crozier, P. A.; Wang, R.; Sharma, R. In Situ Environmental TEM Studies of Dynamic Changes in Cerium-Based Oxides Nanoparticles during Redox Processes. *Ultramicroscopy* **2008**, *108* (11), 1432–1440.

(17) Zhang, K.; Li, G.; Zou, C.; Chen, S.; Li, S.; Han, Z.-K.; Jiang, Y.; Yuan, W.; Yang, H.; Ganduglia-Pirovano, M. V. A CeO_2(100) Surface Reconstruction Unveiled by in Situ STEM and Particle Swarm Optimization Techniques. *Sci. Adv.* **2024**, *10* (32), eadn7904.

(18) Yuan, W.; Chen, B.; Han, Z.-K.; You, R.; Jiang, Y.; Qi, R.; Li, G.; Wu, H.; Ganduglia-Pirovano, M. V.; Wang, Y. Direct In-Situ Insights into the Asymmetric Surface Reconstruction of Rutile TiO_2(110). *Nat. Commun.* **2024**, *15* (1), 1616.

(19) Yuan, W.; Wang, Y.; Li, H.; Wu, H.; Zhang, Z.; Selloni, A.; Sun, C. Real-Time Observation of Reconstruction Dynamics on TiO_2(001) Surface under Oxygen via an Environmental Transmission Electron Microscope. *Nano Lett.* **2016**, *16* (1), 132–137.

(20) Yuan, W.; Zhu, B.; Li, X.-Y.; Hansen, T. W.; Ou, Y.; Fang, K.; Yang, H.; Zhang, Z.; Wagner, J. B.; Gao, Y. Visualizing H_2O Molecules Reacting at TiO_2 Active Sites with Transmission Electron Microscopy. *Science* **2020**, *367* (6476), 428–430.

(21) Zang, W.; Lee, J.; Tieu, P.; Yan, X.; Graham, G. W.; Tran, I. C.; Wang, P.; Christopher, P.; Pan, X. Distribution of Pt Single Atom Coordination Environments on Anatase TiO_2 Supports Controls Reactivity. *Nat. Commun.* **2024**, *15*, 998.

(22) Yuan, W.; Zhang, D.; Ou, Y.; Fang, K.; Zhu, B.; Yang, H.; Hansen, T. W.; Wagner, J. B.; Zhang, Z.; Gao, Y. Direct

in Situ TEM Visualization and Insight into the Facet-dependent Sintering Behaviors of Gold on TiO_2. *Angew. Chemie* **2018**, *130* (51), 17069–17073.

(23) Varilla, L. A. A.; Seriani, N.; Montoya, J. A. Molecular Adsorption and Dissociation of CO_2 on TiO_2 Anatase (001) Activated by Oxygen Vacancies. *J. Mol. Model.* **2019**, *25* (8), 231.

(24) Kim, K. H.; Choi, C.; Choung, S.; Cho, Y.; Kim, S.; Oh, C.; Lee, K.; Lee, C.; Zhang, K.; Han, J. W. Continuous Oxygen Vacancy Gradient in TiO_2 Photoelectrodes by a Photoelectrochemical-driven "Self-purification" Process. *Adv. Energy Mater.* **2022**, *12* (7), 2103495.

(25) Diebold, U. The Surface Science of Titanium Dioxide. *Surf. Sci. Rep.* **2003**, *48* (5–8), 53–229.

(26) Fang, K.; Li, G.; Ou, Y.; Yuan, W.; Yang, H.; Zhang, Z.; Wang, Y. An Environmental Transmission Electron Microscopy Study of the Stability of the TiO_2(1×4) Reconstructed (001) Surface. *J. Phys. Chem. C* **2019**, *123* (35), 21522–21527.

(27) Yuan, W.; Wu, H.; Li, H.; Dai, Z.; Zhang, Z.; Sun, C.; Wang, Y. In Situ STEM Determination of the Atomic Structure and Reconstruction Mechanism of the TiO_2(001)(1×4) Surface. *Chem. Mater.* **2017**, *29* (7), 3189–3194.

(28) Li, G.; Fang, K.; Ou, Y.; Yuan, W.; Yang, H.; Zhang, Z.; Wang, Y. Surface Study of the Reconstructed Anatase TiO_2(001) Surface. *Prog. Nat. Sci. Mater. Int.* **2021**, *31* (1), 1–13.

(29) Matsubu, J. C.; Zhang, S.; DeRita, L.; Marinkovic, N. S.; Chen, J. G.; Graham, G. W.; Pan, X.; Christopher, P. Adsorbate-Mediated Strong Metal–Support Interactions in Oxide-Supported Rh Catalysts. *Nat. Chem.* **2017**, *9* (2), 120–127.

(30) Sokolović, I.; Reticcioli, M.; Čalkovský, M.; Wagner, M.; Schmid, M.; Franchini, C.; Diebold, U.; Setvín, M. Resolving the Adsorption of Molecular O_2 on the Rutile TiO_2(110) Surface by Noncontact Atomic Force Microscopy. *Proc. Natl. Acad. Sci.* **2020**, *117* (26), 14827–14837.

(31) Lee, Y.; Chen, X.; Gericke, S.; Li, M.; Zakharov, D.; Head, A.; Yang, J.; Alexandrova, A. Machine-Learning-Driven Exploration of Surface Reconstructions of Reduced Rutile TiO_2. *ChemRxiv.* **2024**.

(32) Rodriguez, J. A.; Hanson, J. C.; Stacchiola, D.; Senanayake, S. D. In Situ/Operando Studies for the Production of Hydrogen through the Water-Gas Shift on Metal Oxide Catalysts. *Phys. Chem. Chem. Phys.* **2013**, *15* (29), 12004–12025.

(33) Sun, X.; Wu, D.; Zhu, W.; Chen, X.; Sharma, R.; Yang, J. C.; Zhou, G. Atomic Origin of the Autocatalytic Reduction of Monoclinic CuO in a Hydrogen Atmosphere. *J. Phys. Chem. Lett.* **2021**, *12* (39), 9547–9556.

(34) Han, B.; Guo, Y.; Huang, Y.; Xi, W.; Xu, J.; Luo, J.; Qi, H.; Ren, Y.; Liu, X.; Qiao, B. Strong Metal–Support Interactions between Pt Single Atoms and TiO_2. *Angew. Chemie Int. Ed.* **2020**, *59* (29), 11824–11829.

(35) DeRita, L.; Resasco, J.; Dai, S.; Boubnov, A.; Thang, H. V.; Hoffman, A. S.; Ro, I.; Graham, G. W.; Bare, S. R.; Pacchioni, G.; Pan, X.; Christopher, P. Structural Evolution of Atomically Dispersed Pt Catalysts Dictates Reactivity. *Nat. Mater.* **2019**, *18*, 746–751.

(36) Kresse, G.; Joubert, D. From Ultrasoft Pseudopotentials to the Projector Augmented-Wave Method. *Phys. Rev. B* **1999**, *59*, 1758.

(37) Kresse, G.; Hafner, J. Ab Initio Molecular Dynamics for Liquid Metals. *Phys. Rev. B* **1993**, *47* (1), 558–561.

(38) Kresse, G.; Furthmüller, J. Efficient Iterative Schemes for Ab Initio Total-Energy Calculations Using a Plane-Wave Basis Set. *Phys. Rev. B* **1996**, *54* (16), 11169.

(39) Perdew, J. P.; Burke, K.; Ernzerhof, M. Generalized Gradient Approximation Made Simple. *Phys. Rev. Lett.* **1996**, *77* (18), 3865.

(40) Tkatchenko, A.; Scheffler, M. Accurate Molecular Van Der Waals Interactions from Ground-State Electron Density and Free-Atom Reference Data. *Phys. Rev. Lett.* **2009**, *102* (7), 73005.

(41) Dudarev, S. L.; Botton, G. A.; Savrasov, S. Y.; Humphreys, C. J.; Sutton, A. P. Electron-Energy-Loss Spectra and the Structural Stability of Nickel Oxide: An LSDA+ U Study. *Phys. Rev. B* **1998**, *57* (3), 1505.

(42) Haa, M.-A.; Alexandrova, A. N. Oxygen Vacancies of Anatase (101): Extreme Sensitivity to the Density Functional Theory Method. *J. Chem. Theory Comput.* **2016**, *12* (6), 2889–2895.

(43) Liu, J.-Y.; Gong, X.-Q.; Alexandrova, A. N. Mechanism of CO_2 Photocatalytic Reduction to Methane and Methanol on Defected Anatase TiO_2 (101): A Density Functional Theory Study. *J. Phys. Chem. C* **2019**, *123* (6), 3505–3511.

(44) Batatia, I.; Batzner, S.; Kovács, D. P.; Musaelian, A.; Simm, G. N. C.; Drautz, R.; Ortner, C.; Kozinsky, B.; Csányi, G. The Design Space of e (3)-Equivariant Atom-Centered Interatomic Potentials. *arXiv Prepr. arXiv2205.06643* **2022**.

(45) Jain, A.; Ong, S. P.; Hautier, G.; Chen, W.; Richards, W. D.; Dacek, S.; Cholia, S.; Gunter, D.; Skinner, D.; Ceder, G. Commentary: The Materials Project: A Materials Genome Approach to Accelerating Materials Innovation. *APL Mater.* **2013**, *1* (1), 011002.

(46) Batatia, I.; Benner, P.; Chiang, Y.; Elena, A. M.; Kovács, D. P.; Riebesell, J.; Advincula, X. R.; Asta, M.; Avaylon, M.; Baldwin, W. J. A Foundation Model for Atomistic Materials Chemistry. *arXiv Prepr. arXiv2401.00096* **2023**.

(47) Zhang, Z.; Gee, W.; Lavroff, R. H.; Alexandrova, A. N. GOCIA: A Grand Canonical Global Optimizer for Clusters,

Interfaces, and Adsorbates. *Phys. Chem. Chem. Phys.* **2025**, *27* (2), 696–706.

(48) Sun, Q.; Reuter, K.; Scheffler, M. Effect of a Humid Environment on the Surface Structure of RuO_2 (110). *Phys. Rev. B* **2003**, *67* (20), 205424.

(49) Zhai, H.; Alexandrova, A. N. Ensemble-Average Representation of Pt Clusters in Conditions of Catalysis Accessed through GPU Accelerated Deep Neural Network Fitting Global Optimization. *J. Chem. Theory Comput.* **2016**, *12* (12), 6213–6226.

(50) Deaven, D. M.; Ho, K.-M. Molecular Geometry Optimization with a Genetic Algorithm. *Phys. Rev. Lett.* **1995**, *75* (2), 288.

(51) Lee, T.; Soon, A. The Rise of Ab Initio Surface Thermodynamics. *Nat. Catal.* **2024**, *7* (1), 4–6.

(52) Sun, G.; Alexandrova, A. N.; Sautet, P. Structural Rearrangements of Subnanometer Cu Oxide Clusters Govern Catalytic Oxidation. *ACS Catal.* **2020**, *10* (9), 5309–5317.